Carbon 228 (2024) 119371

Contents lists available at ScienceDirect

Carbon

journal homepage: www.elsevier.com/locate/carbon

Research paper

Quantitative measurement of graphitic sp^2 on single nanodiamonds with sub-monolayer sensitivity using differential interference contrast and photo-thermal microscopy

Samuel Hamilton [a], David Regan [a], Lukas Payne [a,b], Paola Borri [a], Wolfgang Langbein [b,*]

[a] School of Biosciences, Cardiff University, Museum Avenue, CF10 3AX, Cardiff, UK
[b] School of Physics and Astronomy, Cardiff University, The Parade, CF24 3AA, Cardiff, UK

ARTICLE INFO

Dataset link: https://doi.org/10.17035/d.2024.0325515217

Keywords:
Nanodiamonds
Graphite
Surface
Photothermal microscopy
Differential interference contrast
sp2-sp3 bond
Single particle

ABSTRACT

The surface of nanodiamonds is prone to be decorated with a graphitic layer due to the thermodynamic instability of diamond versus graphite. Notably, this surface layer affects the zeta-potential of nanodiamonds controlling their colloidal stability, modulates the charging of embedded nitrogen vacancy centres used for sensing and quantum technology, and introduces an optical absorption which leads to heating and destruction of nanodiamonds under intense laser irradiation. Physical and chemical treatments to reduce the graphitic carbon are available, but a sensitive method to measure this graphitic layer on single nanodiamonds is lacking. Here, we demonstrate a non-destructive method to quantitatively determine the graphitic carbon correlatively with the nanodiamond size, on individual nanodiamonds. The method allows determining the fraction of graphitic sp^2 to diamond sp^3 bonded atoms, and estimating the sp^2 surface layer thickness. We investigated milled nanodiamonds, both untreated and chemically treated to remove sp^2. We found that untreated nanodiamonds were covered by the equivalent of a single sp^2 monolayer, which was reduced to 10% of a monolayer for treated nanodiamonds. In both cases, significant variations between individual nanodiamonds were observed. The minimum number of sp^2 bonded atoms detectable under the measurement conditions reported here was found to be 2×10^4.

1. Introduction

Nanodiamonds (NDs) are of significant present interest owing to their mechanical, chemical, electrical and optical properties, making them useful in a broad range of fields including abrasive machining, electrochemistry, quantum technology and medicine [1]. Particularly for medical applications, the low cytotoxicity of sp^3 carbon and the facile functionalisation of the ND surface make them candidates for drug delivery, while implanted nitrogen vacancy centres (NV) can be used as bio-trackers and sensors [2,3]. Similarly, due to the quantum properties of these implanted NV centres, it has been shown that NDs containing them can be utilised for quantum metrology applications such as magnetometry [4].

The surface of NDs is often covered with a graphitic layer, typically formed during synthesis due to the thermodynamic instability of diamond versus graphite. NDs can be produced synthetically in a variety of ways such as by chemical vapour deposition (CVD), by detonation, or by high pressure high temperature (HPHT) synthesis. Most similar to the conditions of natural diamond formation, HPHT synthesis is carried out at temperatures of between 2000 °C and 4000 °C with pressures of around 15 GPa, and graphite is typically used as the precursor material [5]. The temperature and pressure conditions required for HPHT can be lowered to around 1300 °C and 5 GPa with the use of catalysts such as nickel, iron, or cobalt, though the introduction of these materials can lead to metallic impurities in the diamonds produced [6,7]. CVD growth of diamond is achieved by the use of gases containing hydrogen, carbon, and oxygen from which a plasma is generated either by the use of a hot filament at 1700 °C or by microwaves maintaining the plasma by impact ionisation [8,9]. CVD uses pressures below 10 kPa, where graphite is the stable phase, and diamond growth is selected by etching graphitic carbon with hydrogen in a narrow growth parameter window [10]. Synthesis of NDs by detonation results in high levels of surface graphite. This is because after the detonation of explosives in a sealed container generating high temperatures and pressures allowing for diamond formation [11], graphitic carbon is the stable phase during the cool-down and is formed on the NDs [12]. Surface treatment methods to remove such graphitic

* Corresponding author.
E-mail address: langbeinww@cardiff.ac.uk (W. Langbein).

https://doi.org/10.1016/j.carbon.2024.119371
Received 4 March 2024; Received in revised form 7 June 2024; Accepted 18 June 2024
Available online 24 June 2024

shells, as well as other defects caused by various synthesis methods, have been developed. Wet chemistry methods include using acid baths as well as strong liquid oxidants, which can be hazardous and costly due to the corrosive nature of the chemicals used. There are also dry chemistry procedures, including catalyst assisted oxidation and ozone enriched air oxidation [13]. However, also these require the use of harmful chemicals and can cause contamination of the NDs. Alternatively, air annealing of NDs has been shown to remove the sp^2 carbon present due to different oxidation rates of sp^2 and sp^3 bonded atoms [14,15].

Notably, the sp^2 surface layer does not only change the surface chemistry but also introduces an optical absorption which leads to heating and destruction of NDs under intense laser irradiation [16]. Moreover, the presence of surface sp^2 suppresses the fluorescence of NV containing NDs [17] due to the conversion of charged NV^- to neutral NV^0 centres [18]. Surface sp^2 has also been shown to affect the zeta potential of NDs due to protonation of sp^2, causing a net positive charge and increasing the basicity of the surrounding water [19]. Furthermore, sp^2 can lead to the generation of reactive oxygen species, increasing the cytotoxicity of the NDs [20].

In order to fully harness the application benefits of NDs, it is therefore important to quantify their sp^2 surface contamination with high accuracy and sensitivity, ideally on individual NDs to avoid ensemble averaging effects. Reported methods to measure sp^2 in diamond are Raman spectroscopy [21,22] or X-ray photoelectron spectroscopy (XPS) [23,24]. Both are limited to diamond films or ND ensemble studies. Moreover, XPS is sensitive only down to a few nanometers below the sample surface. High-resolution transmission electron microscopy (HRTEM) can be used to distinguish diamond and graphitic lattices, and has been used to study the transformation of NDs to carbon onions [25,26]. However, it is costly and not able to identify surface coverages below a monolayer. Tip-enhanced Raman microscopy [27] was also used to study this transformation resolving clusters of small NDs, but not reporting sp^2 quantification.

Here, we present a simple, non-destructive optical method to quantitatively determine the amount of graphitic carbon correlatively with the size of individual NDs. The method allows us to determine the sp^2/sp^3 fraction and to estimate the sp^2 surface layer thickness, with single particle sensitivity.

2. Methods

2.1. Samples

NDs were purchased with nominal size ranges of 0–50 nm, 0–150 nm, and 0–250 nm (MSY 0–0.05 μm, 0–0.15 μm, and 0–0.25 μm, Microdiamant, Switzerland). They are monocrystalline diamond powders produced by high-pressure high-temperature (HPHT) synthesis. The size distribution and shape of the MSY 0–0.05 has been investigated with TEM in [28], and a range of MSY sizes were used to investigate spin coherence times as function of particle size [29]. More details on the size and shape characterisation of these NDs is given in the supplement Sec. S1. As well as investigating the NDs as purchased, samples were treated to reduce the surface sp^2. This treatment consisted in immersing NDs in concentrated sulphuric acid for 2 h, followed by air annealing at 600 °C for 5 h.

All coverslips and microscope slides were cleaned before use. This was achieved by immersing them in toluene and sonicating for 20 min, followed by immersion in acetone and sonication for another 20 min, and then immersion in deionised water and boiling for 3 min. Finally, slides and coverslips were immersed in 30% hydrogen peroxide and sonicated for 20 min, then stored in a fridge in hydrogen peroxide until needed.

For optical microscopy, NDs were dispersed in water to concentrations of 10^7 particles/ml for the 0–250 nm, samples, and 10^9 particles/ml for the 0–50 nm and 0–150 nm samples. The dispersions were then sonicated to break apart aggregates, before being deposited onto (24×24) mm^2 #1.5 coverslips (Menzel Gläser) by drop casting 10 μl of the dispersion and drying while covered to avoid contamination using a hot plate at 60 °C. The NDs were then immersed in silicone oil (Sigma Aldrich, AP 150 Wacker) of refractive index $n = 1.51$ by pipetting 20 μl of oil onto the coverslip surface. A microscope slide was added and squeezed, with the excess oil wiped away using a clean room wipe, and the borders were sealed using clear nail varnish.

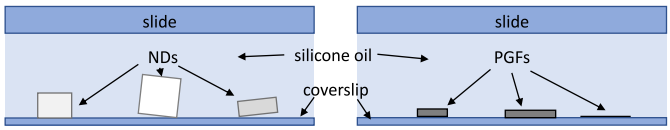

Fig. 1. Sketches of the sample geometries for nanodiamonds (left) and graphene flakes (right) encapsulated between coverslip and slide immersed in silicone oil.

In order to calibrate photothermal (PT) microscopy, pristine graphene flakes (PGFs) with nominal sizes of 500 nm dispersed in ethanol were purchased from Graphene Supermarket. The stock dispersion with a nominal concentration of 1.2×10^{18} PGFs/ml was diluted in ethanol to a concentration of 10^{12} PGFs/ml and 10 μl of the dispersion was drop cast onto a coverslip. The remainder of the sample preparation was the same as for the NDs. A sketch of the geometry of both ND and PGF samples is shown in Fig. 1 for illustration.

2.2. Optical setups

Quantitative differential interference contrast (qDIC) was used to measure the sizes of the NDs, photothermal (PT) microscopy was used to obtain the sp^2 content of the NDs and PGFs, and extinction microscopy was used to measure the sizes of the PGFs.

2.2.1. qDIC

Details of the qDIC setup and data analysis are provided in [30]. The setup is based on a Nikon Ti-U inverted microscope stand. A 100 W tungsten lamp (V2-A LL 100 W, Nikon) was used for illumination with a green interference filter (GIF, Nikon) and a coloured glass filter (BG40, Schott), to select an illumination with a peak wavelength λ of 550 nm and 53 nm full width at half maximum (FWHM). A de-Sénarmont compensator, consisting of a linear polariser followed by a quarter-wave plate (T-P2 DIC Polariser HT MEN51941, Nikon), was used to control the phase offset between the two linear light polarisation components which are split by a Nomarski prism (Nikon N2 DIC module MEH52500) in direction, and focussed onto the sample using an oil-immersion condenser (HNAO MEL41410, Nikon) of 1.34 numerical aperture (NA), yielding a shear distance of 238 nm. A 1.45 NA 100× oil-immersion objective (Nikon MRD01905) was used for imaging. A second Nomarski prism (Nikon N2 DIC slider MBH76190) recombined the beams, followed by a linear polariser (Nikon Ti-A-E DIC analyser block MEN 51980). A 1× tube lens formed an image on a CCD camera (Hamamatsu Orca 285) with 18,000 electrons full well capacity, 7 electrons read noise, 4.6 electrons per count, 12 bit digitiser, 1344 × 1024 pixels and pixel size 6.45 μm. For each dataset a total of $N_a = 256$ averages were obtained with an exposure time of 120 ms. Polariser angles of $\theta = 15$ degrees were used, yielding a phase offset of $\psi = 30$ degrees with images obtained at positive and negative angles for qDIC. The corresponding quantitative analysis is described in detail in Hamilton et al. [30]. Briefly, the qDIC contrast provides the differential phase images $\delta(\mathbf{r})$, from which the integrated phase images $\phi(\mathbf{r})$ are retrieved, using Wiener-filtering with a signal to noise parameter κ. The measured phase area A_ϕ^{m} is then obtained by the spatial integral of $\phi(\mathbf{r})$ over a circular region centred at a selected particle position with radius of r_i, and using as background phase the average over the ring region from r_i to $2r_\mathrm{i}$.

For the setup used, the choice of $\kappa = 200$ and $r_i = 4$ pixels provides a balance between systematic error and signal to noise ratio (SNR) [30]. A correction factor $\rho = 1.25$ was then applied to A_ϕ^{m} to take into account the systematic error of the integration procedure, and provide the integrated phase area, $A_\phi = \rho A_\phi^{\mathrm{m}}$ which has been shown to give accurate sizes for dielectric nanoparticles [30]. The volume V of a dielectric particle of refractive index n_{p} surrounded by a medium of refractive index n_{m} can then be determined as

$$V = \frac{\lambda A_\phi}{2\pi(n_{\mathrm{p}} - n_{\mathrm{m}})}. \tag{1}$$

Assuming a cubic geometry of the NDs, the cube edge length is given by $S = \sqrt[3]{V}$.

2.2.2. Extinction microscopy

Details of the extinction setup and data analysis are provided in Payne et al. [31,32]. Briefly, extinction images were obtained using a second Nikon Ti-U microscope stand. Again a 100 W halogen lamp (Nikon V2-A LL 100 W) was used for illumination, but here a bandpass filter (thorlabs FB550-40) and a neutral colour balance filter (Nikon NCB) were used to provide an illumination wavelength range of (550 ± 20) nm. In addition to unpolarised illumination, radially polarised illumination was created by a home-built radial polariser [33] in the collimated beam path to the oil-immersion condenser (Nikon HNAO MEL41410) of 1.34 NA, to increase the out of plane polarisation component at the sample. A 1.45 NA 100× oil-immersion objective (Nikon MRD01905) and a 1× tube lens was used for imaging the transmitted light onto a scientific-CMOS camera (PCO Edge 5.5 RS) with a 16 bit digitiser, 2560 × 2160 pixels, pixel size $d_{\mathrm{px}} = 6.5\,\mu$m, full well capacity N_{fw}= 30,000 electrons, 2 electrons read noise, and 0.54 electrons per count. For the measurements obtained using the radial polariser, the condenser NA range below 1.0 was blocked to achieve higher out-of plane polarisation components. For referencing, the sample was shifted between two positions 1.4 μm apart in the x-direction every 128 averages. This allowed a shifted referencing method to be used for analysis of σ_{ext} as described in Payne et al. [31,32]. A total of N_{a}= 12800 averages per image were obtained, which yielded a measurement shot noise of $\hat{\sigma}_{\mathrm{ext}}$=3 nm^2 for the extinction cross-section σ_{ext} of individual particles, as calculated using the expression [31]

$$\hat{\sigma}_{\mathrm{ext}} = \frac{3\lambda d_{\mathrm{px}}}{2M\mathrm{NA}}\sqrt{\frac{\pi}{N_{\mathrm{a}}N_{\mathrm{fw}}}}, \tag{2}$$

where M and NA are the magnification and numerical aperture of the objective, respectively.

2.2.3. Photothermal microscopy

In PT imaging [34], a probe beam is modulated by the localised heating of the sample under investigation, induced by the absorption of an heating beam. The modulation of the probe beam is then measured, as reviewed in Adhikari et al. [35]. In our experiments, the PT measurements were acquired using a stimulated Raman scattering microscopy setup described in Langbein et al. [36]. A Ti:sapphire laser source (Spectra Physics MaiTai HP) providing optical pulses of 150 fs duration at 80 MHz repetition rate centred at 820 nm wavelength was used as pump for stimulated Raman loss (SRL), at the same time acting as probe for PT microscopy. The frequency doubled Ti:sapphire output pumped an optical parametric oscillator (Radiantis Inspire HF 100), providing an idler beam with pulses of similar duration and tuneable centre wavelength across 950–1200 nm, which was used as Stokes beam in SRL and acts as heating beam in PT. The Stokes beam was passed through an acousto-optic modulator (AOM) to square-wave amplitude modulate the beam at $\nu_{\mathrm{m}} = 2.5$ MHz with a duty cycle of 50%. The beam then traversed a motorised optical delay line before combining with the pump beam at a dichroic beam splitter. Glass blocks in the beam path were used to control the linear chirp of the pulses for spectral focussing [36]. The beam was scanned by x-y galvo mirrors

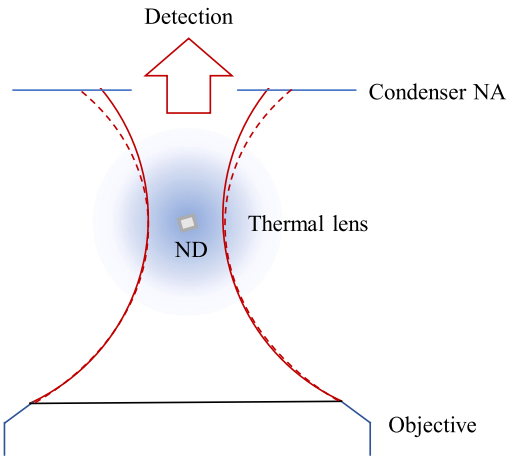

Fig. 2. Sketch showing the effect of photothermal lensing, caused by the absorption of the idler beam from a particle in silicone oil. The dashed/solid lines indicate the beam with/without the defocussing PT lens expected for silicone oil assuming a thermooptic coefficient dn/dT around -3×10^{-4}/K [37]. The coverslip glass has a much lower coefficient of the order of 10^{-6}/K [38] which can be neglected. A modulated detection results from the variable clipping at the condenser lens, in the collection beam path.

relayed into the objective back focal plane. The same microscope stand, objective and condensor as in the extinction microscopy were used. The condensor collected the transmitted beam, as seen in Fig. 2. The Stokes beam was then separated from the pump using a dichroic (Thorlabs DMLP900R) and a shortpass filter (Semrock FF01-945/SP). The pump beam was detected by a photodiode (Hamamatsu S6967) with 86% quantum efficiency at 820 nm, using a home built 2.5 MHz resonant circuit with a DC impedance of $Z_{\mathrm{dc}} = 3.6\,\Omega$, and a resonant impedance of $Z_{\mathrm{li}} = 10$ kΩ. The resulting voltage was amplified by 10 and analysed using a dual channel lock-in amplifier (Zurich Instruments HF2LI) synchronised to the AOM amplitude modulation, to retrieve the transmitted pump beam intensity modulation.

Vibrationally-resonant SRL in the silicone oil mounting medium was used to align the beams, in terms of their spatial, directional and temporal pulse overlap, and to determine the modulation phase of a signal corresponding to an instantaneous loss mechanism. The Stokes was set to 1080 nm central wavelength, and spectral focussing was adjusted via glass blocks to provide a pulse duration of 1.12 ps and a spectral resolution of 34 cm^{-1}. Silicone oil has a vibrational resonance at 2904 cm^{-1} which was used to calibrate the pump-Stokes delay. A spectrum is shown in Fig. 3. We note that the Raman resonances of diamond at 1332 cm^{-1} and of ordered graphite at 1575 cm^{-1} are outside the accessible wavenumber range. The second-order Raman peaks of graphite around 3250 cm^{-1} and 2700 cm^{-1}are accessible but are not resonant for the chosen Stokes wavelength. The phase of the silicone oil SRL signal at 2904 cm^{-1} was set to zero using the lock-in offset phase, indicating no phase shift between modulation and signal. To suppress vibrationally-resonant SRL and perform PT measurements, the delay between the Stokes and pump beams was increased to 2.7 ps, hence beyond pulse overlap, with the Stokes beam arriving first. The absorption of the Stokes by the sp^2 in the sample causes heating of the surrounding medium, thus changing its refractive index, which then results in a modulation of the pump beam. Notably, the PT time constants are much larger than the pulse repetition period, so that the PT lens is accumulated over the 16 pulses in each on/off segment of the 2.5 MHz AOM modulation at the 80 MHz repetition rate. The dual channel lock-in provides the in-phase and in-quadrature components, denoted here as the real, $\Re$, and imaginary, $\Im$, components of the signal, respectively, providing the complex PT signal $S_{\mathrm{li}} = |S_{\mathrm{li}}|\exp(i\phi)$, with the phase ϕ.

For quantitative PT image analysis, we determine, for each bright spot in the PT image, the spatial integral of S_{li} over the spot area, in

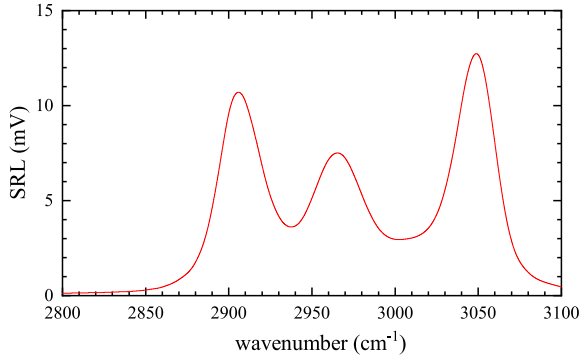

Fig. 3. SRL spectrum of silicone oil, showing the vibrational resonances in the CH stretch region and the peak at 2904 cm^{-1}.

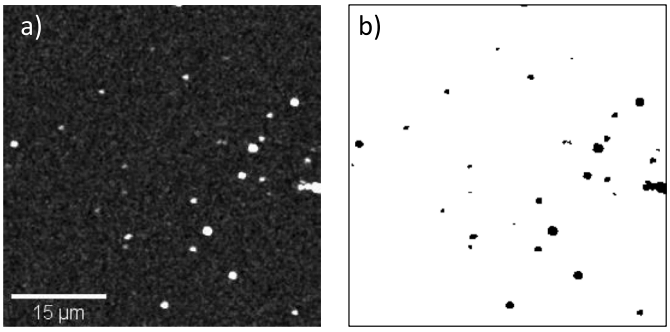

Fig. 4. Photothermal image of the untreated NDs with nominal sizes up to 250 nm. (a) Gray scale from m = 0 mV (black) to M = 0.3 mV (white). (b) Mask applied for the analysis of the areal integrals A_{li} at each spot.

order to provide high signal to noise and reduce systematics. This was done manually for each spot, choosing a region, as can been seen in Fig. 4, over which S_{li} was integrated to yield A_{li}.

The DC signal S_{dc} from the photodiode was also acquired and is used to determine the relative modulation M_r at the centre of the point spread function (PSF) as $M_r = A_{li} Z_{dc}/(A_p S_{dc} Z_{li})$. The effective PSF area $A_p = (0.26\,\mu m)^2$ used for this scaling was determined from the ratio between A_{li} and the value of S_{li} at the peak for typical measurements, and could vary between $(0.1\,\mu m)^2$ to $(0.5\,\mu m)^2$ for different peaks.

The phase ϕ of the signal was used to extract an effective exponential PT signal decay time, as it is known from frequency domain lifetime imaging [39,40], yielding an effective PT lifetime of $\tau = \tan(\phi)/(\pi \nu_m)$. We note that the actual dynamics of the PT signal is non-exponential [34,41].

3. Experimental results on single nanodiamonds

3.1. Optimising the condenser NA

PT detection relies on converting the thermal lens around the heat source into a modulation of the detected signal. Here we detect the transmitted pump beam power, which is collected by the condenser. Since the PT lens is changing the divergence of the transmitted beam, one can choose the detected NA to maximise the signal to noise. For very low NA, most of the power is blocked, reducing the signal to noise due to the increasing relative intensity shot noise. For very high NA instead, essentially all transmitted light is detected, and the change of divergence by the PT lens has little effect. Thus we expect that the optimum NA is around the point where half of the transmitted beam is collected, as also suggested by previous reports [41,42]. To find the optimum NA experimentally, measurements were carried out on individual NDs, imaging the same region at various values for the

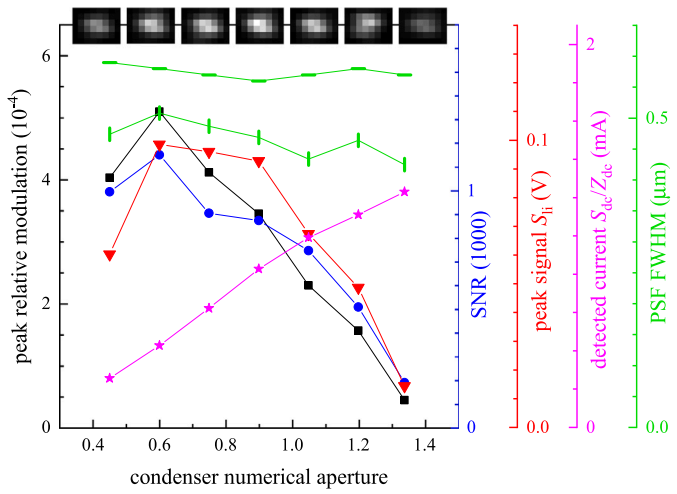

Fig. 5. Influence of the condenser NA on PT imaging contrast for a representative ND. The peak relative modulation $|M_r|$ (squares), the signal to noise ratio (circles), the peak PT signal (triangles), the detected current (stars), and the FWHM of the PSF (bars) are shown, referring to the respective scales given. PT images (linear grey scale from m = 0 to M = 2.6 mV; size $(1.51 \times 1.13)\ \mu m^2$) of the ND are given for each NA values measured. The width of the PSF is fitted with a Gaussian profile at the given NA, both vertically and horizontally, as indicated by the direction of the bar symbols. Pump and Stokes powers are 5.4 mW and 2.5 mW, respectively, measured at the microscope beam entrance; measurements are acquired using 0.2 µm pixel size and 2 ms dwell time.

condenser NA between 0.45 NA and 1.34 NA. Fig. 5 shows the resulting NA dependence of the detected current S_{dc}/Z_{dc}, and for a single representative ND the peak modulation $|S_{li}|$, the relative modulation $|M_r|$, and the signal to noise ratio (SNR) calculated as $|S_{li}|/\sigma_{li}$ using the standard deviation σ_{li} of S_{li} in background regions.

Reducing the NA from the maximum of 1.34 NA increases $|S_{li}|$ by up to a factor of 7, with a broad maximum around 0.7 NA. The $|S_{li}|$ maximum occurs when about half of the transmitted probe power is detected (as shown by S_{dc}/Z_{dc}). Accordingly, the SNR curve is shifted to slightly smaller NA, due to the decreasing shot noise in the detected current. Similarly $|M_r|$ has a maximum at a slightly lower NA around 0.6, due to the decreasing detected current. Fully opening the condenser to 1.34 NA decreases the SNR by an order of magnitude from its maximum, showing that high NA collection is advantageous for SRS microscopy where PT signals are unwanted background. The PSF size is nearly independent of NA, showing only a small increase of around 10% when decreasing the condenser NA. This weak dependence on collection NA is expected, as the PT signal is governed by the focussed excitation beams which are unaffected. A more detailed discussion of the underlying theory is given in Selmke [41]. The smaller size along the vertical compared to the horizontal direction originates from the linear polarisation of pump and Stokes beams in the horizontal direction, and the high NA of the focussing objective. A similar behaviour was observed for all particles in the region analysed. In the following sections, 0.6 NA was used for PT measurements.

3.2. Correlative qDIC and PT measurements

In order to quantify the graphitic layer thickness of a single ND, one needs to know both the ND size and the number of sp^2 bonded atoms. Assuming a dominant diamond (sp^3) fraction of the ND volume, we can use qDIC with a particle refractive index of bulk diamond to determine the ND size, as given in Eq. (1). Conversely, the PT signal reports the amount of sp^2 of the ND. Indeed, sp^3 diamond is transparent for the Stokes wavelength around 1100 nm and thus does not contribute to PT heating, while sp^2 is absorptive. The PT signal was calibrated using PGFs of known absorption cross-section, as determined by single particle extinction microscopy (see Section 4 below). Following calibration,

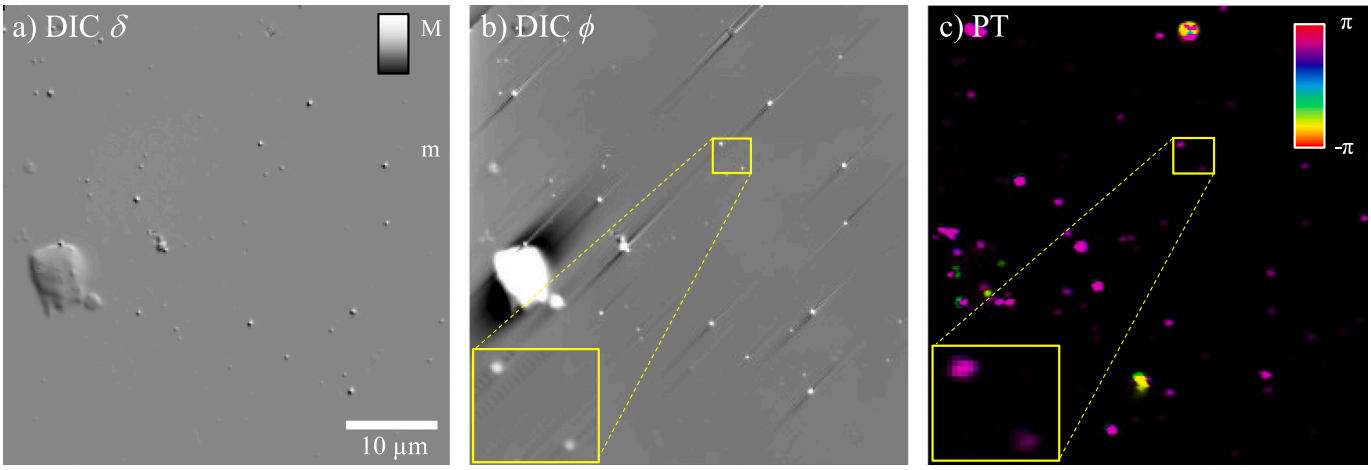

Fig. 6. qDIC and PT images of the untreated NDs of nominal sizes up to 250 nm. (a) Differential phase $\delta(\vec{r})$ on a grey scale as shown, from $m = -0.1$ rad to $M = 0.1$ rad. The shadow cast impression of DIC is evident, with the shear $s = 0.238(1, 1)/\sqrt{2}$ µm in the (x, y) coordinates (x horizontal, y vertical). (b) Corresponding phase $\phi(\vec{r})$ image ($m = -0.1$ rad to $M = 0.1$ rad), with an inset showing a region of (3.94×3.55) µm^2 around selected particles indicated by the yellow square ($m = -0.18$ rad to $M = 0.18$ rad) using Wiener filtering with $\kappa = 200$. (c) PT image S_{ti} of the same region using a HSV colour map at maximum saturation with the value range 0 to 1 encoding PT signal amplitudes 0 to 4 mV and a hue given by the PT signal phase ($-\pi$ to π radians) as shown. The inset shows a zoom of a selected region of (4.53×3.96) µm^2 around the same particles as in b, using a 0 to 3 mV amplitude range. (For interpretation of the references to colour in this figure legend, the reader is referred to the web version of this article.)

the PT signal gives a quantitative measure of the number of sp^2 bonds on the ND surface.

Fig. 6a and b show qDIC images of a region on the untreated NDs with nominal sizes up to 250 nm. The typical shadow cast pattern can be seen in the differential $\delta(\mathbf{r})$ image, which converts to a peak pattern in the $\phi(\mathbf{r})$ image after the integration by Wiener filtering. The stripes along the shear direction around each peak are artefacts of the Wiener integration and have an extension determined by the signal to noise parameter κ [30]. The corresponding PT image is given in Fig. 6c, using a hue-saturation-value (HSV) colour scale, with a value given by the amplitude and a hue by the phase, as indicated. The insets in Fig. 6b and c exemplify that the same NDs are visible in qDIC and PT, indicating that these NDs have sp^2 bonded carbon in their structure.

To gain a quantitative measurement of the sp^2 on individual NDs, the following analysis was carried out. Firstly, the volume V of the NDs was determined by qDIC, as described in Section 2.2.1. Assuming a cubic shape, the surface area is given by $A = 6V^{2/3}$. The peak relative modulation M_r is expected to be proportional to the number of sp^2 bonds, which scales with the surface area assuming a given surface density of sp^2 bonds. The measured dependence of M_r on A across the ensemble is given in Fig. 7, showing an approximate proportionality as expected, but with a significant spread of the corresponding scaling factor between different NDs. This indicates that the sp^2 amount varies significantly between NDs in the ensemble, instead of being a defined homogeneous sp^2 layer of given thickness. We also find that the treatment described in Section 2.1 reduced the amount of sp^2. The average scaling factors between the area A and $|M_r|$ have been determined evaluating the mean of $\log(A/|M_r|)$ and its error. This results in a scaling factor $(2.4 \pm 0.4) \times 10^{-10}$ nm^{-2} for untreated and $(1.17 \pm 0.16) \times 10^{-10}$ nm^{-2} for treated NDs, hence different within error, and shown as lines in Fig. 7.

We note that assuming the NDs are cubic is a simplification which can create systematic errors. For more realistic shapes (see SEM images in the Supplementary Information Sec. S1), the aspect ratio is typically 2:1 between longest and shortest dimension. This would lead to a relative increase of surface by only 5%–6%, and for an aspect ratio of 4:1 by 19% to 26%. Since moreover the shapes are not exactly rectangular, we estimate that the surface area can be up to twice the one of a cube shape. This variability of the surface area for a given volume will affect the correlation between absorption and volume in Fig. 7.

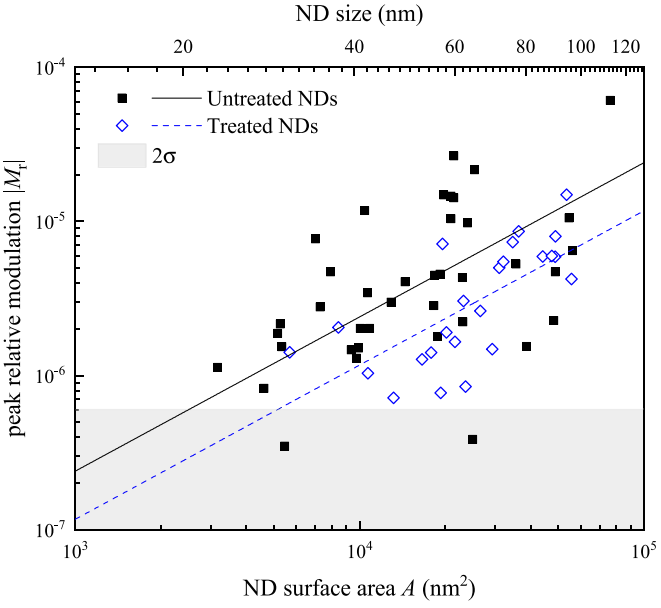

Fig. 7. Correlation between the ND surface area A calculated from the ND volume measured in qDIC assuming cubic shape, and the peak relative modulation $|M_r|$ measured in PT and attributed to sp^2 bonds. Data for both the untreated (filled squares) and treated (open diamonds) ND samples are shown. Solid (dashed) lines show average scaling factors for untreated (treated) samples. The grey shaded region shows the noise (two standard deviations σ) of M_r.

Interestingly, we also found that the treated NDs could withstand higher laser powers. In turn, as detailed in Sec. S2, this allowed us to measure coherent anti-Stokes Raman scattering from individual NDs which were smaller than in our previous work [16], without observing their degradation, consistent with a reduced amount of surface sp^2 upon treatment.

3.3. Photothermal sensitivity

The sensitivity of the qDIC technique for the phase area A_ϕ has been determined previously [30] to be around 17 nm^2, corresponding

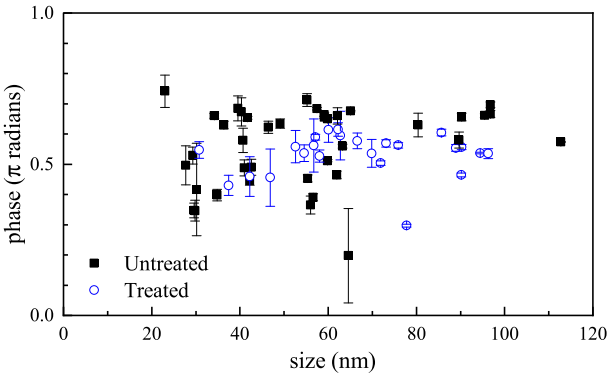

Fig. 8. PT signal A_{li} phase for all measured treated (circles) and untreated (squares) NDs versus their size. The error bars are determined from the noise of A_{li}.

to a ND with a size of around 12 nm for the conditions used here. Conversely, the sensitivity of the PT technique needs to be established. This was done by analysing a large number of positions with no NDs present for each region imaged, yielding a noise of standard deviation (σ) of 29 μV for each quadrature of S_{li} with a condenser NA of 0.6 and a pixel dwell time of 2 ms. This equates to a σ of 41 μV nm^2 in A_{li} and 3.1×10^{-7} in M_r. In order to ensure that the analysed peaks are well above the noise, only peaks of $|M_r|$ higher than 2σ were analysed, that is $|M_r| > 6.1 \times 10^{-7}$. This limit is shown in Fig. 7 as grey area. Powers of $P_s = 2.4$ mW and $P_p = 5$ mW at the microscope beam entrance were used for the Stokes and pump beams, respectively, for all results shown. These were chosen to be just below the threshold of detaching or graphitising the studied NDs, see also [16]. For this reason, increasing PT sensitivity by using higher laser powers is problematic. On the other hand, since the signal is shot-noise limited, longer pixel dwell times τ_p and smaller pixel sizes s_p allow for more sensitive measurements, noting that M_r is scaling as P_s and σ of M_r is scaling as $s_p/\sqrt{P_p \tau_p}$.

3.4. Photothermal phase and lifetime

The phase of A_{li} for the set of NDs measured is shown in Fig. 8. We find a variation of the phase around $\pi/2$, within ±0.3 rad. A phase of $\pi/2$ relates to a lifetime much longer than the modulation period of 400 ns. This is as expected, from the PT signal response time of several μs for the focus size used in our experiments [34,41].

4. Determination of sp^2 bond numbers

To determine the number of sp^2 bonded atoms from the PT signal, we use graphene nanoflakes as calibration sample. These are strong absorbers and weak scatters, allowing us to measure their absorption cross-section on a single particle basis using extinction microscopy [31]. Furthermore, graphene has a known and constant absorption throughout the near infrared, so that the absorption cross-section can be used to determine the flake area and the corresponding number of sp^2 bonds. Then, measuring the PT signal on the same nanoflake, the PT signal strength, which is proportional to the absorption cross-section [35], can be calibrated in units of number of sp^2 bonded atoms. Note that such a procedure is not viable directly on the NDs since they are strong scatters and weak absorbers, so that the determination of the absorption cross-section from extinction microscopy is not accurate. A combination of exctinction and scattering microscopy, in principle, can be used to separate scattering and absorption cross-sections [43]. However, this is not reliable for weak absorbers, as the absorption cross-section is then the difference between two large values, extinction and scattering cross-sections, which both have errors [44,45].

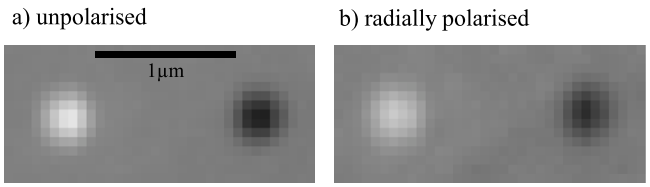

Fig. 9. Extinction images showing a region of (2.20×0.97) μm^2 around an individual PGF (from $m = -0.02$ to $M = 0.02$) when using (a) unpolarised or (b) radially polarised light.

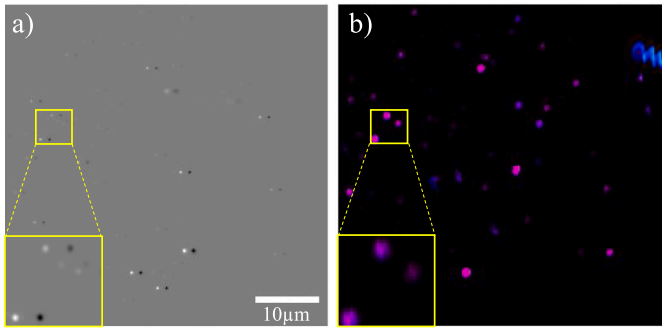

Fig. 10. (a) Extinction image of a region on the PGF sample (from $m = -0.1$ to $M = 0.1$,), with an inset showing a (4.97×4.61) μm^2 region around the particles shown in the yellow square ($m = -0.08$ to $M = 0.08$). Unpolarised illumination. (b) PT image S_{li} showing the same region as (a) (m = 0 mV to M = 10 mV) with the phase encoded as an HSV colour as in Fig. 7, and an inset showing the same particles as in the inset for (a) (5.47×5.28) μm^2 ($m = 0$ mV to $M = 40$ mV). (For interpretation of the references to colour in this figure legend, the reader is referred to the web version of this article.)

In vacuum, the absorption of a graphene layer η_{gr} is given by [46] $\pi\alpha = 2.3\%$, where α is the fine-structure constant. This is reduced in a medium by the refractive index, in the present case 1.51, yielding an absorption of $\eta_{gr} = 1.5\%$. For single layer graphene flakes we thus expect a peak extinction of around 1.5% for in-plane polarisation. For unpolarised illumination over 0–1.34 NA, the axially polarised intensity is weak [33], about 17%, while for radial polarised illumination over 1.0–1.34 NA, the axial component is strong [33], about 58%. For the particles analysed, we found a peak extinction between 0.8% and 1.5% for unpolarised illumination. For radially polarised illumination, some decrease in the peak extinction was seen, however, not as much as would be expected from a single graphene flake. This discrepancy can be attributed to the long shadow effect [47], which yields a measured cross-section that is increased by factor of about 1.25 for the 0–1.34 NA and about 1.6 for 1.0–1.34 NA. Taking into account these factors, the expected measured extinction of a single graphene layer is $1.5\% \times 1.25 \times (100-17)\% = 1.6\%$ for unpolarised and $1.5\% \times 1.6 \times (100-58)\% = 1.0\%$ for radially polarised illumination. Extinction images of an individual PGF of retrieved size $\sqrt{A_{gr}} = 323$ nm are provided in Fig. 9, showing a peak extinction of 1.5% for unpolarised illumination and 1.1% for radially polarised illumination, consistent with this expectation.

Representative unpolarised extinction and PT images obtained on the PGF sample are shown in Fig. 10a and b, respectively. As in Fig. 6, the PT phase has been encoded as a colour map with the PT amplitude. To determine which particles seen in the extinction image were single graphene flakes lying flat on the substrate, line profiles were taken along the particles to show their peak extinction. Only those with a peak extinction between 0.8% and 3% for unpolarised illumination, and a reduced extinction for radially polarised illumination, were deemed to be graphene flakes, and analysed further.

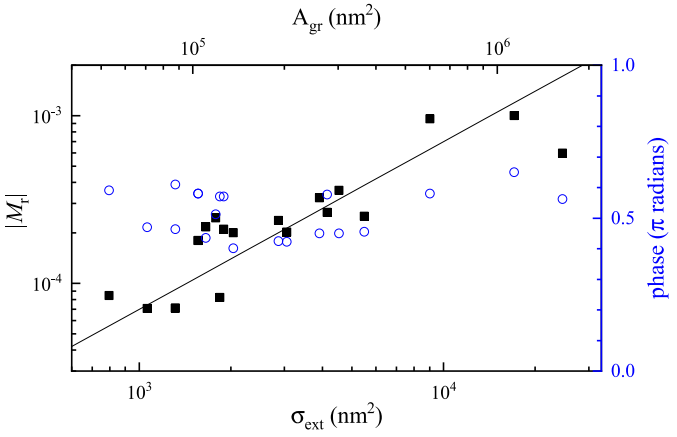

Fig. 11. Peak relative modulation $|M_r|$ (squares) versus extinction cross-section σ_{ext} measured on graphene nanoflakes. The line shows the scaling $|M_r| = \beta\sigma_{ext}$. The corresponding graphene area $A_{gr} = \sigma_{ext}/\eta_{gr}$ is shown on the top axis. The phase of M_r is shown as circles.

A home built ImageJ plugin, Extinction Suite[1], was used to determine the extinction cross section σ_{ext} of the individual absorbing particles. The graphene area of the flakes A_{gr} can then be determined from σ_{ext} as $A_{gr} = \sigma_{ext}/\eta_{gr}$. The peak relative modulation M_r of the particles was found in the same way as for the NDs in Section 3, and is correlated in Fig. 11 with σ_{ext} and the corresponding graphene area A_{gr}. We find that the measured M_r is proportional to σ_{ext}, as expected for the PT signal, within variations by a factor of about two around the average scaling shown by the line $|M_r| = \beta\sigma_{ext}$ with $\beta = 7\times10^{-8}$ nm^{-2}. The observed variations from the scaling could be due to varying geometries of the flakes, which change the shape of the PT lensing. From the resulting graphene area $A_{gr} = |M_r|/(\beta\eta_{gr})$ we can determine the number N_{sp^2} of sp^2 bonded atoms considering that the unit cell of graphene contains two atoms in an area of $A_u = 0.052$ nm^2, yielding $N_{sp^2} = 2A_{gr}/A_u$. The phase of the modulation also shown in Fig. 11 is similar to the PT signal of the NDs shown in Fig. 8, varying around $\pi/2$ as expected.

The observed variations within a factor of two provide an estimate of the accuracy of the method. Furthermore, sp^2 absorption depends on the polarisation relative to the bond direction, so that a strongly orientated bond coverage could result in additional systematic errors.

We note that apart from graphene-type layers on NDs, diamond can show a surface reconstruction of the {111} surfaces providing chains of sp^2 bonded carbon atoms known as Pandey chains [48]. The absorption of such chains has been calculated using density-functional theory simulating vacancy disks [49]. An absorption around 0.05/cm (see Fig. 7 of [49]) is reported between 1.5 eV and 2.5 eV photon energy, for a vacancy density of 1.52×10^{17} cm^{-3}. This corresponds to a cross-section of $\sigma_v = 3.3\times10^{-5}$ nm^2 per vacancy, and since there are two vacancies per sp^2 bond (see Fig. 3 of [49]), to a cross-section of $\sigma_{sp^2} = 6.6\times10^{-5}$ nm^2 per sp^2 bond. For {110} surfaces, the surface reconstruction can form similar chains, and the absorption (see Fig. 12 of [49]) at 1.5 eV photon energy is about twice higher. Again, there is one sp^2 bond for two vacancies (see Fig. 10 of [49]), yielding $\sigma_{sp^2} \approx 1.3\times10^{-4}$ nm^2 per sp^2 bond. Now, for graphene, there is one sp^2 bond per atom, so that $\sigma_{sp^2} = \eta_{gr}A_u/2 = 3.9\times10^{-4}$ nm^2. This is a few times larger than for the diamond surface reconstructions mentioned above, likely due to the two-dimensional bond network in graphene compared to the one-dimensional chains of the surface reconstructions. Since a Pandey reconstructed {111} diamond surface uses about 0.06 nm^2 per bond [48], it provides an absorption of 0.11% at 1.5 eV. This is equivalent to 0.07 of the graphene flake absorption η_{gr}, and thus would be measured in our method as 7% of a graphene monolayer coverage The heating beam used in our experiments has a photon energy of 1.15 eV, which is not covered in Fig. 12 of [49], but the weak wavelength dependence of the absorption suggests that the above conclusions are still applicable.

[1] http://langsrv.astro.cf.ac.uk/Crosssection

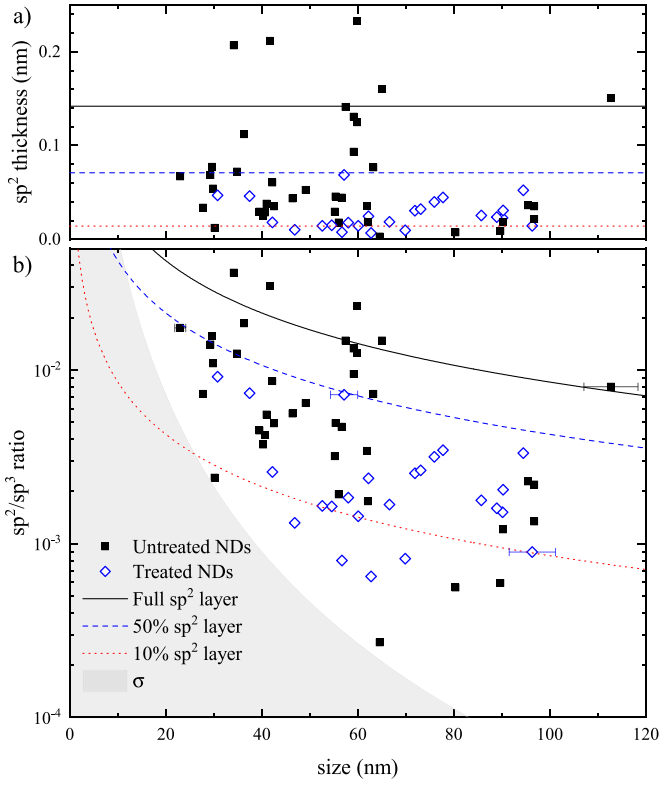

Fig. 12. Thickness t of sp^2 (a), and ratio ρ of the number of sp^2 to sp^3 bonded atoms (b) for individual untreated (squares) and treated (diamonds) NDs versus size. Lines showing the ratios corresponding to different graphene monolayer coverages are shown - 100% (solid), 50% (dashed), and 10% (dotted). The grey shaded region indicates a ratio below the PT noise σ in $|M_r|$.

5. sp^2/sp^3 ratio and sp^2 thickness

Having measured the number of sp^2 bonded atoms for a ND using the calibrated PT signal, and the ND volume using qDIC, we can determine the sp^2/sp^3 atom number ratio for individual NDs. We convert the ND volume V into the number N_{sp^3} of sp^3 bonded atoms considering that a cubic unit cell of diamond of volume $V_u = 0.045$ nm^3 contains 8 atoms, so that the number of sp^3 atoms in a volume V of diamond is given by $N_{sp^3} = 8V/V_u$. The ratio of sp^2 to sp^3 atoms is then $\rho = N_{sp^2}/N_{sp^3} = |M_r|V_u/(8\beta\eta_{gr}A_uS^3)$, and is shown in Fig. 12b versus the ND size. In general the earlier observations still hold, with the untreated NDs containing a higher number of sp^2 atoms compared to treated NDs.

Assuming that the sp^2 atoms are located at the ND surface, we can determine the thickness t of the sp^2 layer as follows. For small thicknesses compared to the ND sizes, we can consider the volume of sp^2 bonds in a ND as $t(6S^2) = \rho S^3$, where $6S^2$ is the ND surface area and S^3 the volume, yielding $t = \rho S/6$. The resulting thicknesses are given in Fig. 12a. For comparison we show in Fig. 12b curves of constant sp^2 thickness calculated as $\rho = 6t/S$, with $t = 0.142$ nm for a full monolayer. We can see that the treated NDs have 5%–30% sp^2 monolayer coverage, while the untreated NDs have a very variable coverage, up to about 150%.

We recall that a Pandey reconstruction of the surfaces results in an absorption corresponding to 7% sp^2 monolayer coverage as discussed

above, which is close to some of the data found (see red line indicating 10% coverage in Fig. 12a).

The sensitivity limit of the present PT measurements can be estimated using $\sigma = 3.1 \times 10^{-7}$ noise in $|M_r|$, and is shown as grey area in Fig. 12b. It corresponds to a number of $N_{sp^2} = 2\sigma/(\beta\eta_{gr}A_u) \approx 2 \times 10^4$ sp^2-bonded atoms.

6. Conclusion

In conclusion, we have presented a sensitive method to determine the size of single nanodiamonds correlatively with their surface graphitisation, expressed as the sp^2/sp^3 ratio, using a combination of qDIC and PT microscopy. NDs fabricated using HPHT synthesis and milled to size where investigated, either untreated, or treated to remove sp^2 using sulphuric acid and air annealing. We found that, on average, treated NDs had a sp^2 content corresponding to a surface coverage by a sp^2 monolayer, while treated NDs had a significantly reduced sp^2 content, corresponding to some 10% surface coverage, in both cases showing strong variations between individual NDs. The minimum number of sp^2 atoms detectable in PT imaging was 2×10^4, which corresponds to a monolayer coverage for a ND of about 10 nm size.

With the rising interest in the use of NDs across many fields, from medicine to quantum technologies, it becomes increasingly important to develop sensitive methods able to quantify their sp^2 content. Indeed, the presence of sp^2 is a serious drawback, e.g. leading to the graphitisation of NDs over time under optical excitation [16], and affecting the spectral stability of NV centres [17,50] in quantum technology applications. The presented method offers a way to quantitatively determine the sp^2 content at the single ND level using optical microscopy instrumentation, applicable e.g. for bench-top quality control of individual NDs in future manufacturing.

CRediT authorship contribution statement

Samuel Hamilton: Writing – review & editing, Writing – original draft, Visualization, Validation, Methodology, Investigation, Formal analysis, Data curation. **David Regan:** Writing – review & editing, Software, Methodology. **Lukas Payne:** Writing – review & editing, Software. **Paola Borri:** Writing – review & editing, Validation, Supervision, Project administration, Methodology, Funding acquisition, Conceptualization. **Wolfgang Langbein:** Writing – review & editing, Writing – original draft, Visualization, Validation, Supervision, Software, Resources, Project administration, Methodology, Funding acquisition, Conceptualization.

Declaration of competing interest

The authors declare that they have no known competing financial interests or personal relationships that could have appeared to influence the work reported in this paper.

Data availability

Information on the data underpinning the results presented here, including how to access them, can be found in the Cardiff University data catalogue at https://doi.org/10.17035/d.2024.0325515217.

Acknowledgements

S.H. acknowledges support for his PhD studies by the EPSRC Diamond Science and Technology CDT grant EP/L015315/1 and Cardiff University, United Kingdom. The microscope equipment was supported by the EPSRC grants EP/I005072/1 and EP/M028313/1. We acknowledge Dr Joseph Bleddyn Williams for contributing to the development of the qDIC analysis software. We thank Dr Iestyn Pope for contributions to the microscope setup and technical support. We thank Prof Oliver Williams, Prof Phil Davies, and Ryan Lewis for contributions to the ND treatment, and Ryan Lewis and Dr Iestyn Pope for CARS measurements.

Appendix A. Supplementary data

Supplementary material related to this article can be found online at https://doi.org/10.1016/j.carbon.2024.119371.

References

[1] K. Turcheniuk, V.N. Mochalin, Biomedical applications of nanodiamond (review), Nanotechnology 28 (2017) 252001.
[2] H. Zhu, Y. Wang, A. Hussain, Z. Zhang, Y. Shen, S. Guo, Nanodiamond mediated co-delivery of doxorubicin and malaridine to maximize synergistic anti-tumor effects on multi-drug resistant mcf-7/adr cells, J. Mater. Chem. B 5 (2017) 3531–3540.
[3] F. Morales-Zavala, N. Casanova-Morales, R.B. Gonzalez, A. Chandía-Cristi, L.D. Estrada, I. Alvizú, V. Waselowski, F. Guzman, S. Guerrero, M. Oyarzún-Olave, et al., Functionalization of stable fluorescent nanodiamonds towards reliable detection of biomarkers for alzheimer's disease, J. Nanobiotechnol. 16 (2018) 1–14.
[4] S. Pezzagna, B. Naydenov, F. Jelezko, J. Wrachtrup, J. Meijer, Creation efficiency of nitrogen-vacancy centres in diamond, New J. Phys. 12 (2010) 065017.
[5] S. Eaton-Magaña, J.E. Shigley, C.M. Breeding, Observations on HPHT-grown synthetic diamonds: A review, Gems Gemolog. 53 (2017) 262–284.
[6] L.-W. Yin, N.-W. Wang, Z.-D. Zou, M.-S. Li, D.-S. Sun, P.-Z. Zheng, Z.-Y. Yao, Formation and crystal structure of metallic inclusions in a HPHT as-grown diamond single crystal, Appl. Phys. A 71 (2000) 473–476.
[7] Z. Liang, X. Jia, C. Zang, P. Zhu, H. Ma, G. Ren, The influences of n and h on diamond synthesized with ni−mn−co catalyst by HPHT, Diam. Relat. Mater. 14 (2005) 243–247.
[8] G.-R. Lai, E. Farabaugh, A. Feldman, L. Robins, Deposition of diamond films in a closed hot filament cvd system, J. Res. Nat. Inst. Stand. Technol. 100 (1995) 43.
[9] T. Mitomo, T. Ohta, E. Kondoh, K. Ohtsuka, An investigation of product distributions in microwave plasma for diamond growth, J. Appl. Phys. 70 (1991) 4532–4539.
[10] P. Gautama, H. Toyota, Y. Iwamoto, X. Zhu, S. Nomura, S. Mukasa, Synthesizing diamond film on cu, fe and si substrate by in-liquid microwave plasma cvd, Precis. Eng. 49 (2017) 412–420.
[11] K. Iakoubovskii, M. Baidakova, B. Wouters, A. Stesmans, G. Adriaenssens, A. Vul', P. Grobet, Structure and defects of detonation synthesis nanodiamond, Diam. Relat. Mater. 9 (2000) 861–865.
[12] G.V. Sakovich, A.S. Zharkov, E.A. Petrov, Results of research into the physicochemical processes of detonation synthesis and nanodiamond applications, Nanotechnol. Russ. 8 (2013) 581–591.
[13] E. Mayerhoefer, A. Krueger, Surface control of nanodiamond: From homogeneous termination to complex functional architectures for biomedical applications, Acc. Chem. Res. 55 (2022) 3594–3604.
[14] S. Stehlik, M. Varga, M. Ledinsky, V. Jirasek, A. Artemenko, H. Kozak, L. Ondic, V. Skakalova, G. Argentero, T. Pennycook, et al., Size and purity control of HPHT nanodiamonds down to 1 nm, J. Phys. Chem. C 119 (2015) 27708–27720.
[15] S. Osswald, G. Yushin, V. Mochalin, S.O. Kucheyev, Y. Gogotsi, Control of sp2/sp3 carbon ratio and surface chemistry of nanodiamond powders by selective oxidation in air, J. Am. Chem. Soc. 128 (2006) 11635–11642.
[16] I. Pope, L. Payne, G. Zoriniants, E. Thomas, O. Williams, P. Watson, W. Langbein, P. Borri, Coherent anti-Stokes Raman scattering microscopy of single nanodiamonds, Nat. Nanotechnol. 9 (2014) 940–946.
[17] C. Bradac, T. Gaebel, C.I. Pakes, J.M. Say, A.V. Zvyagin, J.R. Rabeau, Effect of the nanodiamond host on a nitrogen-vacancy color-centre emission state, Small 9 (2012) 132–139.
[18] M.V. Hauf, B. Grotz, B. Naydenov, M. Dankerl, S. Pezzagna, J. Meijer, F. Jelezko, J. Wrachtrup, M. Stutzmann, F. Reinhard, J.A. Garrido, Chemical control of the charge state of nitrogen-vacancy centers in diamond, Phys. Rev. B 83 (2011) 081304.
[19] L. Ginés, S. Mandal, Ashek-I-Ahmed, C.-L. Cheng, M. Sow, O.A. Williams, Positive zeta potential of nanodiamonds, Nanoscale 9 (2017) 12549–12555.
[20] D.-K. Lee, S. Ha, S. Jeon, J. Jeong, D.-J. Kim, S.W. Lee, W.-S. Cho, The sp^3/sp^2 carbon ratio as a modulator of in vivo and in vitro toxicity of the chemically purified detonation-synthesized nanodiamond via the reactive oxygen species generation, Nanotoxicology 14 (2020) 1213–1226.
[21] W. Fortunato, A. Chiquito, J. Galzerani, J. Moro, Crystalline quality and phase purity of cvd diamond films studied by Raman spectroscopy, J. Mater. Sci. 42 (2007) 7331–7336.
[22] V.I. Korepanov, H.-o. Hamaguchi, E. Osawa, V. Ermolenkov, I.K. Lednev, B.J. Etzold, O. Levinson, B. Zousman, C.P. Epperla, H.-C. Chang, Carbon structure in nanodiamonds elucidated from Raman spectroscopy, Carbon 121 (2017) 322–329.
[23] T. Petit, J.-C. Arnault, H.A. Girard, M. Sennour, P. Bergonzo, Early stages of surface graphitization on nanodiamond probed by X-ray photoelectron spectroscopy, Phys. Rev. B 84 (2011) 233407.

[24] A. Kozakov, A. Kochur, N. Kumar, K. Panda, A. Nikolskii, A. Sidashov, Determination of sp^2 and sp^3 phase fractions on the surface of diamond films from C1s, valence band x-ray photoelectron spectra and CKVV x-ray-excited Auger spectra, Appl. Surf. Sci. 536 (2021) 147807.
[25] O.O. Mykhaylyk, Y.M. Solonin, D.N. Batchelder, R. Brydson, Transformation of nanodiamond into carbon onions: A comparative study by high-resolution transmission electron microscopy, electron energy-loss spectroscopy, X-ray diffraction, small-angle X-ray scattering, and ultraviolet Raman spectroscopy, J. Appl. Phys. 97 (2005) 074302.
[26] M. Zeiger, N. Jäckel, M. Aslan, D. Weingarth, V. Presser, Understanding structure and porosity of nanodiamond-derived carbon onions, Carbon 84 (2015) 584–598.
[27] A. Rosenkranz, L. Freeman, S. Fleischmann, F. Lasserre, Y. Fainman, F.E. Talke, Tip-enhanced Raman spectroscopy studies of nanodiamonds and carbon onions, Carbon 132 (2018) 495–502.
[28] I. Rehor, P. Cigler, Precise estimation of HPHT nanodiamond size distribution based on transmission electron microscopy image analysis, Diam. Relat. Mater. 46 (2014) 21–24.
[29] E. Rej, T. Gaebel, T. Boele, D.E. Waddington, D.J. Reilly, Hyperpolarized nanodiamond with long spin-relaxation times, Nature Commun. 6 (2015) 8459.
[30] S. Hamilton, D. Regan, L. Payne, W. Langbein, P. Borri, Sizing individual dielectric nanoparticles with quantitative differential interference contrast microscopy, Analyst 147 (2022) 1567–1580.
[31] L.M. Payne, W. Langbein, P. Borri, Wide-field imaging of single-nanoparticle extinction with sub-nm^2 sensitivity, Phys. Rev. Appl. 9 (2018) 034006.
[32] L.M. Payne, W. Albrecht, W. Langbein, P. Borri, The optical nanosizer – quantitative size and shape analysis of individual nanoparticles by high-throughput widefield extinction microscopy, Nanoscale 12 (2020) 16215–16228.
[33] F. Alabdullah, V. Singh, L. Payne, D. Regan, F. Masia, V.G. Rocha, W. Langbein, P. Borri, Radially-polarised light in single particle optical extinction microscopy identifies silver nanoplates, Appl. Phys. Lett. 124 (2023) 181105.
[34] S. Berciaud, D. Lasne, G.A. Blab, L. Cognet, B. Lounis, Photothermal heterodyne imaging of individual metallic nanoparticles: Theory versus experiment, Phys. Rev. B 73 (2006) 045424.
[35] S. Adhikari, P. Spaeth, A. Kar, M.D. Baaske, S. Khatua, M. Orrit, Photothermal microscopy: Imaging the optical absorption of single nanoparticles and single molecules, ACS Nano 14 (2020) 16414–16445.
[36] W. Langbein, D. Regan, I. Pope, P. Borri, Heterodyne dual-polarization epi-detected cars microscopy for chemical and topographic imaging of interfaces, APL Photonics 3 (2018) 092402.
[37] R. Kamikawachi, I. Abe, A. Paterno, H. Kalinowski, M. Muller, J. Pinto, J. Fabris, Determination of thermo-optic coefficient in liquids with fiber Bragg grating refractometer, Opt. Commun. 281 (2008) 621–625.
[38] Schott Technical Information, TIE19 Temperature Coefficient of the Refractive Index, Technical Report, Schott, 2016.
[39] M.J. Booth, T. Wilson, Low-cost, frequency-domain, fluorescence lifetime confocal microscopy, J. Microsc. 214 (2004) 36–42.
[40] J.R. Lakowicz, Principles of Fluorescence Spectroscopy, Springer, 1999.
[41] M. Selmke, Photothermal Single Particle Detection in Theory and Experiments (Ph.D. thesis), University of Leipzig, Leibzig, Germany, 2013.
[42] J. Miyazaki, H. Tsurui, K. Kawasumi, T. Kobayashi, Sensitivity enhancement of photothermal microscopy with radially segmented balanced detection, Opt. Lett. 40 (2015) 479.
[43] A. Zilli, W. Langbein, P. Borri, Quantitative measurement of the optical cross sections of single nano-objects by correlative transmission and scattering microspectroscopy, ACS Photonics 6 (2019) 2149–2160.
[44] Y. Wang, A. Zilli, Z. Sztranyovszky, W. Langbein, P. Borri, Quantitative optical microspectroscopy, electron microscopy, and modelling of individual silver nanocubes reveals surface compositional changes at the nanoscale, Nanoscale Adv. 2 (2020) 2485–2496.
[45] Y. Wang, Z. Sztranyovszky, A. Zilli, W. Albrecht, S. Bals, P. Borri, W. Langbein, Quantitatively linking morphology and optical response of individual silver nanohedra, Nanoscale 14 (2022) 11028–11037.
[46] R.R. Nair, P. Blake, A.N. Grigorenko, K.S. Novoselov, T.J. Booth, T. Stauber, N.M.R. Peres, A.K. Geim, Fine structure constant defines visual transparency of graphene, Science 320 (2008) 1308.
[47] L. Payne, A. Zilli, Y. Wang, W. Langbein, P. Borri, Quantitative high-throughput optical sizing of individual colloidal nanoparticles by wide-field imaging extinction microscopy, in: Proc. SPIE 10892, Colloidal Nanoparticles for Biomedical Applications XIV, in: Colloidal Nanoparticles for Biomedical Applications XIV, vol. 10892, 108920J.
[48] K.C. Pandey, New dimerized-chain model for the reconstruction of the diamond (111)-(2 × 1) surface, Phys. Rev. B 25 (1982) 4338–4341.
[49] L.S. Hounsome, R. Jones, P.M. Martineau, D. Fisher, M.J. Shaw, P.R. Briddon, S. Öberg, Origin of brown coloration in diamond, Phys. Rev. B 73 (2006) 125203.
[50] B.R. Smith, D.W. Inglis, B. Sandnes, J.R. Rabeau, A.V. Zvyagin, D. Gruber, C.J. Noble, R. Vogel, E. Ōsawa, T. Plakhotnik, Five-nanometer diamond with luminescent nitrogen-vacancy defect centers, Small 5 (2009) 1649–1653.